RESEARCH ARTICLE

Unsteady turbulent boundary layers in swimming rainbow trout

Kazutaka Yanase* and Pentti Saarenrinne

ABSTRACT

The boundary layers of rainbow trout, *Oncorhynchus mykiss*, swimming at 1.02±0.09 *L* s^{-1} (mean±s.d., *N*=4), were measured by the particle image velocimetry (PIV) technique at a Reynolds number of 4×10^5. The boundary layer profile showed unsteadiness, oscillating above and beneath the classical logarithmic law of the wall with body motion. Across the entire surface regions that were measured, local Reynolds numbers based on momentum thickness, which is the distance that is perpendicular to the fish surface through which the boundary layer momentum flows at free-stream velocity, were greater than the critical value of 320 for the laminar-to-turbulent transition. The skin friction was dampened on the convex surface while the surface was moving towards a free-stream flow and increased on the concave surface while retreating. These observations contradict the result of a previous study using different species swimming by different methods. Boundary layer compression accompanied by an increase in local skin friction was not observed. Thus, the overall results may not support absolutely the Bone–Lighthill boundary layer thinning hypothesis that the undulatory motions of swimming fish cause a large increase in their friction drag because of the compression of the boundary layer. In some cases, marginal flow separation occurred on the convex surface in the relatively anterior surface region, but the separated flow reattached to the fish surface immediately downstream. Therefore, we believe that a severe impact due to induced drag components (i.e. pressure drag) on the swimming performance, an inevitable consequence of flow separation, was avoided.

KEY WORDS: Particle image velocimetry, Boundary layer, Lateral line, *Oncorhynchus mykiss*, Skin friction, Swimming performance

INTRODUCTION

Boundary layer phenomena are ubiquitous in an aquatic environment, where the surface of any biotic or abiotic object is subjected to a flow. When a fluid moves past a solid object, the layer that is immediately next to the surface does not slip relative to the surface. The fluid's velocity increases with increasing surface-normal distance (*y*) and reaches 99% of the free-stream velocity (*U*) at the edge of the boundary layer [δ=*y*(99%*U*); Schlichting, 1979]. Thus, because of a substantial change in flow velocity within a very thin layer, viscous effects become significant in the boundary layer, even though the viscosity of the fluid is small enough for its effects to be negligible in the main flow. Assuming that an inviscid fluid flows along a surface, the solid surface would have to be displaced outwards by a distance δ*, the displacement thickness necessary to maintain the same total mass flow rate as the viscous case

(Schlichting, 1979). Fluid particles in laminar boundary layers travel along neighbouring layers. However, with increasing distance (*x*) from the object's leading edge, the boundary layers in high Reynolds number flows of real fluid (e.g. water) undergo a remarkable transition from a laminar to turbulent regime in which the velocity gradient towards the surface becomes acute. This significantly increases the viscous stress in the layer immediately next to the surface (i.e. viscous sublayer), which is defined as:

$$\tau = \mu \frac{\mathrm{d}u}{\mathrm{d}y}, \tag{1}$$

where μ is the dynamic viscosity of the fluid (Newton's law of friction). In a two-dimensional flow over a curved surface, the fluid moves under the influence of the pressure gradient in the flow direction. In a situation where there is a considerable pressure increase in the downstream direction, which is referred to as an adverse pressure gradient, the combined effect of this and viscous resistance (Eqn 1) causes a significant loss in momentum flux within the boundary layer. Then, the viscous stress at the surface (i.e. the wall shear stress, τ$_0$) may disappear when the momentum of the fluid particle cannot overcome the viscous resistance. Downstream from this point, the boundary layer separates from the surface. The flow direction that is adjacent to the surface then reverses, so that τ$_0$ changes its sign and direction (White, 1991). A significant consequence of flow separation is a large increase in pressure drag.

Skin friction is a major source of resistance to a swimming fish (Webb, 1975). The possibility that compression of the boundary layer due to undulatory swimming motions induces a large increase in the drag forces originating from skin friction is termed the Bone–Lighthill boundary layer thinning hypothesis (Lighthill, 1971). It has long provided a crucial argument for evaluation of the power requirements of aquatic animals during undulatory swimming. However, there was no conclusive evidence for this hypothesis until Anderson et al. (2001) directly measured the fish boundary layer using the particle tracking velocimetry (PTV) technique. The physical demands on the fish in moving forward in a turbulent flow environment are high as a result of the growing mechanical perturbations for coordinated undulatory motion (Pavlov et al., 2000; Webb, 2004a). Given the metabolic benefits of a lowered cost of locomotion for a given swimming speed, and the complex interaction of boundary layers, drag and thrust production, it seems reasonable to assume that active flow sensing by fish could contribute to improving in the efficiency of locomotion. Indeed, active flow sensing by the lateral line has been shown to be important in allowing rainbow trout *Oncorhynchus mykiss* (Walbaum 1792) to modify their rhythmic motor pattern profile (Kármán gait; Liao et al., 2003a). This is a hydrodynamic mechanism that enables rainbow trout to reduce their axial muscle activity, which implies an adaptive response to reduce the cost of locomotion (Liao et al., 2003b). The lateral line of fish consists of two varieties of mechano-receptive organs: superficial neuromasts and canal neuromasts. Both contain mechanosensory hair cells embedded within the epithelium and are

Department of Mechanical Engineering and Industrial Systems, Tampere University of Technology, Korkeakoulunkatu 6, Tampere FI-33101, Finland.

*Author for correspondence (kazutaka.yanase@gmail.com)

List of symbols and abbreviations

B	universal constant, where $B=5.5$
c	travelling body-wave velocity
C_{fx}	local friction coefficient
d	distance from the fish surface to the velocity sampling point
f	oscillatory frequency of the fish surface
H	shape factor
L	body length
l_x	arc-length
PIV	particle image velocimetry
PTV	particle tracking velocimetry
p	pressure
R	vector length
Re	Reynolds number
Re_x	local Reynolds number
Re_θ	momentum thickness Reynolds number
SNR	signal-to noise ratio
T	turbulence intensity
u	tangential velocity
u^+	non-dimensional tangential velocity
U	free-stream velocity
U_e	the maximum tangential flow velocity out of the edge of the boundary layer
u_{rms}	root mean square of the turbulent velocity fluctuations
$U\tau$	friction velocity
V	transverse surface velocity
v	normal velocity
v_w	normal velocity near the surface
v_w^+	non-dimensional normal velocity near the surface
w	normal component of the transverse surface velocity
x	distance from object's leading edge
y	surface-normal distance
y^+	non-dimensional surface-normal distance
α	angle of the fish surface relative to the swimming direction
β	Clauser's parameter
δ	boundary layer thickness
δ^*	displacement thickness
η	dimensionless coordinate where $\eta=y\delta^{-1}$
κ	universal constant, where $\kappa=0.40$
λ	body-wave length
μ	dynamic viscosity of fluid
ν	kinematic viscosity
Π	Coles' wake parameter
θ	momentum thickness
ρ	water density
τ	viscous stress
τ_0	wall shear stress
ϕ	phase

coupled to the cupula, a gelatinous structure. The cupula transmits hydrodynamic forces from the shear flow near these receptors to deflect the hair bundles and, thereby, generates a nervous response (McHenry et al., 2008). Naturally, these specific characteristics lead to an expectation that superficial neuromasts that lie on the external skin surface of the fish are directly deflected as a result of the wall shear stress acting on the fish surface in rhythmic patterns that are associated with body motion.

The present study's fundamental objective was to characterize the unsteady boundary layer phenomena that are caused by the mechanical interaction with the undulatory surface of steadily swimming rainbow trout. Thus, we examined the oscillatory motion-dependent behaviour of boundary layers at various positions on the surface of the fish. The measurements were conducted with the particle image velocimetry (PIV) technique in a flow condition at Reynolds numbers of the order of $Re=4\times10^5$, which suggest a transitional flow regime from laminar to turbulence [the critical values typically are $Re=3.5–5.0(\times10^5)$; Schlichting, 1979]. PIV produces non-intrusive velocity measurements for instantaneous velocity vector fields. It measures flow velocities by illuminating only tracer particles in the plane of interest by an appropriate light source (Raffel et al., 1998). The PIV technique, which is based on statistical correlation of small interrogation areas with a high particle density, offers significant advantages for the direct determination of the surface-normal gradient of longitudinal velocity (Eqn 1) and, hence, wall shear stress in a highly heterogeneous flow field that would otherwise require an indirect means of approximation, such as using an equivalent manmade rigid body. Therefore, the PIV algorithm is more sensitive to the velocity fluctuation component, particularly in transient turbulent boundary layers. However, the PTV is inferior in measuring spatial velocity gradients, because the algorithm uses a relatively sparse seeding. Nevertheless, the PTV algorithm provides a reliable predictor for tracking individual particle images when working with image sequences (cf. single image pair) but it also requires a predictor-corrector scheme to match particles between images (Raffel et al., 1998). In turbulent flows, where there is an entire spectrum of eddies with a wide range of dimensions, the eddies may increase the uncertainty of velocity interpolation in the PTV algorithm. This is due to the low signal-to-noise ratio (SNR) that corresponds to the difference between peak and second peak correlations in cross-correlation-based PIV, and overlapping of particle images (Raffel et al., 1998).

Here, we present boundary layer-related parameters and an overall profile of unsteady boundary layers over the surface of steadily swimming rainbow trout. We compare these measurements with data for different species that have been published by Anderson et al. (2001). This comparison will contribute to a greater understanding of the effect of a species-specific manner of swimming on the mechanical interaction between the propulsive surface and surrounding water, which is responsible for the specific flow behaviour observed. Measurement at one speed in a controlled flow environment with known turbulence intensity will provide a starting point for exploration of the real world in which hydrodynamic disturbances are sensed by the fish.

RESULTS
Boundary layer-related parameters

The surface of rainbow trout (body length $L=0.305\pm0.020$ m, mean±s.d., $N=4$) was divided into three regions based on the arc-length (l_x) of the fish surface measured from the rostrum (Table 1). These regions were: the pectoral region ($l_x=85\pm3$ mm, $N=2$), the pelvic region ($l_x=131\pm18$ mm, $N=3$) and the posterior region ($l_x=207\pm14$ mm, $N=3$). The time averages of the maximum tangential flow velocity out of the edge of the boundary layer that are normalized by the free-stream velocity (U_e/U; Fig. 1A) reached a maximum value of 1.24 ± 0.05 ($N=3$) in the pelvic region when the fish surface was moving towards the free-stream flow (convex-motion phase). This U_e/U value and the 1.19 ± 0.06 U_e/U ($N=3$) in the same surface region, when the fish surface was retreating from the free-stream flow (concave-motion phase), were significantly greater than the 1.05 ± 0.06 U_e/U ($N=4$) over a comparable surface region of the rigid body that had been placed in parallel with the free-stream flow (Tukey's HSD test; d.f.=7, versus convex: $P<0.01$, versus concave: $P<0.05$). There was no statistically significant position-dependent difference in the U_e/U ratio within the same motion phase or rigid body (ANOVA; d.f.=2, 5; $P>0.05$).

The time average of the boundary layer thickness (δ) in the pectoral region (6.00 ± 1.31 mm, $N=2$) in the concave-motion phase significantly exceeded that over the rigid-body surface (1.46 ± 0.37 mm, $N=3$) in a comparable surface region (Tukey's HSD test;

d.f.=4; $P<0.05$; Fig. 1B). However, there was no statistically significant motion-dependent difference of the δ between comparable surface locations in the other surface regions (ANOVA, d.f.=2, 7; $P>0.05$). The colour scales for the velocity field over the rigid-body surface (Fig. 2) illustrate clearly the nature of boundary layer behaviour, in which the thickness increases with increasing l_x (and hence the local Reynolds number, Re_x, based on the l_x). Indeed, a thin boundary layer covers the fish from the head part ($\delta=0.92\pm0.15$ mm, $N=2$) to the pectoral region, although the boundary layer grew rapidly on the posterior half of the rigid-body surface. The δ reached about 10 mm near the tail. The momentum thickness (θ) is an important measure. It represents the distance from the fish surface through which the same momentum that was removed as a result of the presence of the boundary layer could flow. Using θ as a characteristic length scale and U_e as a characteristic velocity scale, the Reynolds numbers (Re_θ) were calculated to be 198 ±107 ($N=2$) in the pectoral region and 671 ± 171 ($N=3$) in the posterior-most region.

The time averages of the wall shear stress (τ_0) were greater in the concave-motion phase than in the convex-motion phase at comparable positions (Fig. 3A). However, a statistically significant difference was detected only in the posterior region (Tukey's HSD test, d.f.=7; $P<0.05$). Flow separation that was determined by a negative τ_0 was observed in five sequences of the convex motion in the pectoral region of a particular fish. It is worth noting that the separating flow reattached to the fish surface immediately downstream in all observations. As Fig. 3B shows, the magnitude of the normal component of surface velocity in the convex-motion phase with flow separation [0.048 ± 0.005 m s^{-1}, number of observations (n)=5] and the neighbouring (i.e. previous and following) concave-motion phases (0.059 ± 0.016 m s^{-1}, $n=5$) was significantly greater than those in the other convex-motion phase (0.024 ± 0.002 m s^{-1}, $n=3$) and concave-motion phase (0.032 ± 0.011 m s^{-1}, $n=3$) in the same region without flow separation (ANOVA; within-convex: $P<0.01$, within-concave: $P<0.05$). In this case, the normal component of the surface velocity (w) is defined as $w=V\cos^{-1}\alpha$, where V is the transverse surface velocity, and α is the angle of the fish surface relative to the swimming direction.

Fig. 4 shows the time averages of the local friction coefficient (C_{fx}), which is defined as $C_{fx}=\tau_0/(0.5\rho U_e^2)$, where ρ is the density of the water, in each of the three surface regions of the swimming fish and rigid body. They are compared with theoretical estimates for a flat plate in the cases of laminar and turbulent boundary layers. The time average of C_{fx} in the posterior region during the concave-motion sequence was significantly greater than that in the same region during the convex-motion sequence (Tukey's HSD test, d.f.=7; $P<0.05$). The C_{fx} values in the pectoral (0.0041 ± 0.0030, $N=3$) anterior region (0.0071 ± 0.0028, $N=2$) at $l_x=38\pm9$ mm on the rigid-body surface are very similar to the flat-plate estimates for the laminar boundary layer.

The distribution wave of the U_e/U ratio, δ, τ_0 and C_{fx} in each of the three surface regions behaved in a manner similar to the out-of-phase wave with body motion. Fig. 5 shows phase (ϕ) of the surface movement in which the maximum and minimum peaks of these parameters were recorded. This phase is indicated by the azimuth projected on the complex plane ($Re^{\phi i}$, where R is the vector length). The maximum τ_0 occurred after the fish surface passed the mid-point ($\phi=\pi$) of the time sequence in the concave-motion phase [pectoral region: 3.66 ± 0.26 rad (210 ± 15 deg), $N=2$; pelvic region: 3.40 ± 0.16 rad (195 ± 9 deg), $N=3$; posterior region: 3.76 ± 0.31 rad (216 ± 18 deg), $N=3$]. The minimum τ_0 occurred around the mid-point ($\phi=0$) of the convex-motion sequence [pectoral region: 6.17 ± 0.04 rad (354 ± 3 deg), $N=2$; pelvic region: 6.03 ± 0.83 rad (346 ± 48 deg), $N=3$; posterior region: 0.30 ± 0.26 rad (17 ± 15 deg), $N=3$]. The peak U_e/U ratio was roughly π out of phase with the other parameters. C_{fx} and δ were roughly in phase with τ_0. However, it is important to note that there was a case (fish 2 in the posterior region; Table 1) where the ϕ for the maximum and minimum δ did not show significant one-sidedness [maximum δ: $\phi=0.32e^{(3.27\pm1.39)i}$, $z=1.13<z_{crit}(\alpha=0.05)=2.92$; minimum δ: $\phi=0.30e^{(6.09\pm1.52)i}$, $z=0.89<z_{crit}(\alpha=0.05)=2.93$; number of observations (n)=11; the Rayleigh test; Batschelet, 1981].

Flow separation profile

Fig. 6 compares the temporal variation in the average τ_0 in the pectoral region during one complete cycle of transverse surface movement of the fish with and without flow separation. The data plots for the fish with flow separation correspond to the plots

Table 1. PIV image acquisition conditions

Surface region	Fish ID	Reference point (%L)	l_x (mm)	Re_x	No. of data sets		
					Convex*	Concave*	Rigid body
Pectoral	1	1 (28%L)	90	2.9×10⁴	5	5	
	3	1 (31%L)	81	3.1×10⁴	3	3	
		(29±2%L)	85±3	3.0×10⁴	8	8	
Pectoral	1–3		79±3	2.8×10⁴			4
Pelvic	1	2 (46%L)	114	4.3×10⁴	2	2	
	2	2 (44%L)	150	5.2×10⁴	2	1	
	4	2 (47%L)	129	4.7×10⁴	1	1	
		(46±2%L)	131±18	4.7×10⁴	5	4	
Pelvic	1–4		137±13	4.6×10⁴			4
Posterior	1	5 (66%L)	203	6.1×10⁴	3	2	
	2	4 (65%L)	223	7.0×10⁴	10	11	
	3	4 (68%L)	195	6.9×10⁴	2	2	
		(66±2%L)	207±14	6.7×10⁴	15	15	
Posterior	1–4		221±12	6.8×10⁴			11
				Grand total	28	27	19

PIV, particle image velocimetry; L, total body length; l_x, arc-length on the fish surface measured from the rostrum; Re_x, Reynolds number based on the arc-length. Reference point: 1, tip of pectoral fin; 2, base of pelvic fin; 3, tip of pelvic fin; 4, anal; 5, base of anal fin. The reference point is also given as a percentage of L: fish 1, 0.277 m; fish 2, 0.304 m; fish 3, 0.318 m; fish 4, 0.320 m.
Where data from more than one fish are shown, mean (±s.d.) values and total number of data sets are also given.
*One complete cycle was a combination of consecutive full 'convex' and 'concave' motions.
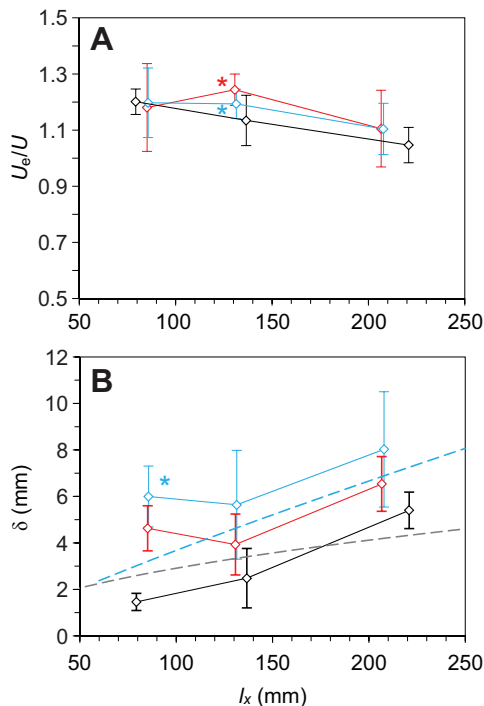
Fig. 1. Relative increases in the near-field flow velocity to the free-stream velocity (U_e/U) and boundary layer thickness (δ) measured at three body regions. Data points from left to right represent pectoral, pelvic and posterior regions. The plots compare (A) the maximum flow velocity out of the edge of the boundary layer normalized by the free-stream velocity (U_e/U) and (B) the boundary layer thickness (δ) between swimming fish in the convex-motion phase (red; pectoral: $N=2$, pelvic: $N=3$, posterior: $N=3$), the concave-motion phase (blue; pectoral: $N=2$, pelvic: $N=3$, posterior: $N=3$) and the rigid body case (black; pectoral: $N=3$, pelvic: $N=4$, posterior: $N=4$). Convex-motion phase versus rigid-body case: red asterisk, significant at $P<0.01$. Concave-motion phase versus rigid-body case: blue asterisk, significant at $P<0.05$. The grey and blue dashed lines represent δ of a flat plate estimated theoretically assuming laminar and turbulent boundary layers, respectively. The error bars represent s.d. from the mean. The local Reynolds numbers, Re_x, based on the arc-length (l_x) of the fish surface from the rostrum are 2.9×10^4 in the pectoral region, 4.6×10^4 in the pelvic region and 6.7×10^4 in the posterior region.

denoted by red and blue circles in Fig. 3B. As Fig. 6 shows, the τ_0 recorded negative values during flow separation, but then returned to a positive range, suggesting a separation-and-reattachment phenomenon. Fig. 7 shows the sequential images of the velocity vector field that were selected from the five convex-motion sequences with flow separation. Fig. 7A shows the image of the velocity vector field when the flow separation was first identified by negative τ_0 in the oscillatory cycle. The separation point, which may lie slightly upstream of $l_x=81$ mm, was not determined because it was outside of the imaged area. The tangential velocity (u) and normal velocity (v) profiles in Fig. 7A show that a small recirculation region with clockwise vortex (counter-clockwise in the velocity vector field image) reached $l_x=91$ mm, where τ_0 was nearly zero. Consequently, this was assumed to be the reattachment point. A negative value for v at the edge of the detached shear layer (distance from surface to 99% free-stream velocity) reveals that there was a net normal flow of fluid from the free stream into the boundary layer. The size of the recirculation region was minimized nine frames after the flow separation was first identified (Fig. 7B). The recirculation region eventually vanished (Fig. 7C). The positive value of v near the fish surface (Fig. 7C) reveals a wall injection

characteristic that was found consistently in the intermediate to later phase of the convex-motion sequence without separation across the surface regions.

Oscillatory boundary layer profile

The displacement thickness (δ*), as one may recall, represents a virtual distance by which the fish surface must be displaced outwards to yield the same flow rate of an inviscid flow at free-stream velocity. The ratio of δ* to the momentum thickness (θ), which is known as the shape factor (H), is used to evaluate unknown boundary layers for their proximity to a laminar or turbulent boundary layer profile. H was independent of l_x (regression analysis, $P>0.05$) in both the convex-motion (1.62 ± 0.07, $N=8$) and concave-motion sequences (1.56 ± 0.09, $N=8$). The momentum thickness Reynolds number (Re_θ) was independent of l_x (regression analysis, $P>0.05$) in both the convex-motion (760 ± 360, $N=8$) and concave-motion phases (789 ± 294, $N=8$).

Unlike what Anderson et al. (2001) observed, the u profiles of rainbow trout agreed poorly with the known laminar boundary layer profile, such as the Falkner–Skan solution. In turbulent boundary layer research based on the classical law of the wall (von Kármán, 1930), the tangential velocity, u, and distance normal to the fish surface, y, are non-dimensionalized as $u^+=uU_\tau^{-1}$ and $y^+=yU_\tau\nu^{-1}$, respectively, by the friction velocity, U_τ. U_τ is defined as $U_\tau=(\tau_0\rho^{-1})^{0.5}$ where ν is the water's kinematic viscosity and ρ is its density. Fig. 8 shows the u^+ profile envelope for a selected sequence of the transverse surface movement in the posterior region. The mean u^+ profile that was determined from a series of five image pairs in the beginning phase of the convex-motion sequence appears in Fig. 8A. In it, the mean u^+ profile in the layer that is close to the fish surface (the viscous sub-layer: $0<y^+<4–5$) approximated the linear law ($y^+=u^+$) and was connected to the buffer layer that is described by Spalding's inner law expression (1961):

$$y^+ = u^+ + e^{-\kappa B}\left[e^{\kappa u^+} - 1 - \kappa u^+ - \frac{(\kappa u^+)^2}{2} - \frac{(\kappa u^+)^3}{6}\right], \quad (2)$$

where κ and B are universal constants for which $\kappa=0.40$ and $B=5.5$ are the values that are used in this paper. Meanwhile, in a series of 18 subsequent image pairs (100 Hz) of the fish surface moving towards the opposite peak of oscillation, the mean u^+ profile (Fig. 8A) at distances further than $y^+=5$ still followed the linear law $y^+=u^+$ until y^+ reached approximately 12 ($y\approx1.1$ mm). Of particular interest is that this mean u^+ profile for $y^+>12$ shows characteristics that are similar to the polymeric sublayer, which is known as Virk's asymptote: $u^+=11.7\ln y^+−17$ (Virk, 1975). Virk's asymptote describes an empirically observed limit to drag reduction caused by adding high molecular weight polymers to wall-bounded turbulent flows. Virk's asymptote pushes the log-law away from the surface, as illustrated by the line $u^+=0.41^{-1}\ln y^++5.0+\Delta u^+$ [$\Delta u^+=10.5\pm4.5$, number of image pairs (n)=18; Fig. 8A]. The average τ_0 during this period was 0.130 ± 0.006 Pa ($n=18$), and U_τ approached zero (0.0114 ± 0.0012, $n=18$). Hence, u^+ became very large relative to the increase in y^+. It is worth noting that a wake-like structure extended into the internal boundary layer ($y^+<\delta=74\pm19$, $n=18$).

In the beginning of the concave-motion phase (Fig. 8B), a mean u^+ profile similar to that observed in the later phase of the convex-motion sequence was continued briefly for a series of four image pairs ($n=4$) at 100 Hz. The mean u^+ profile at greater distances from the fish surface ($y^+>13$) returned to a law-of-the-wall-like
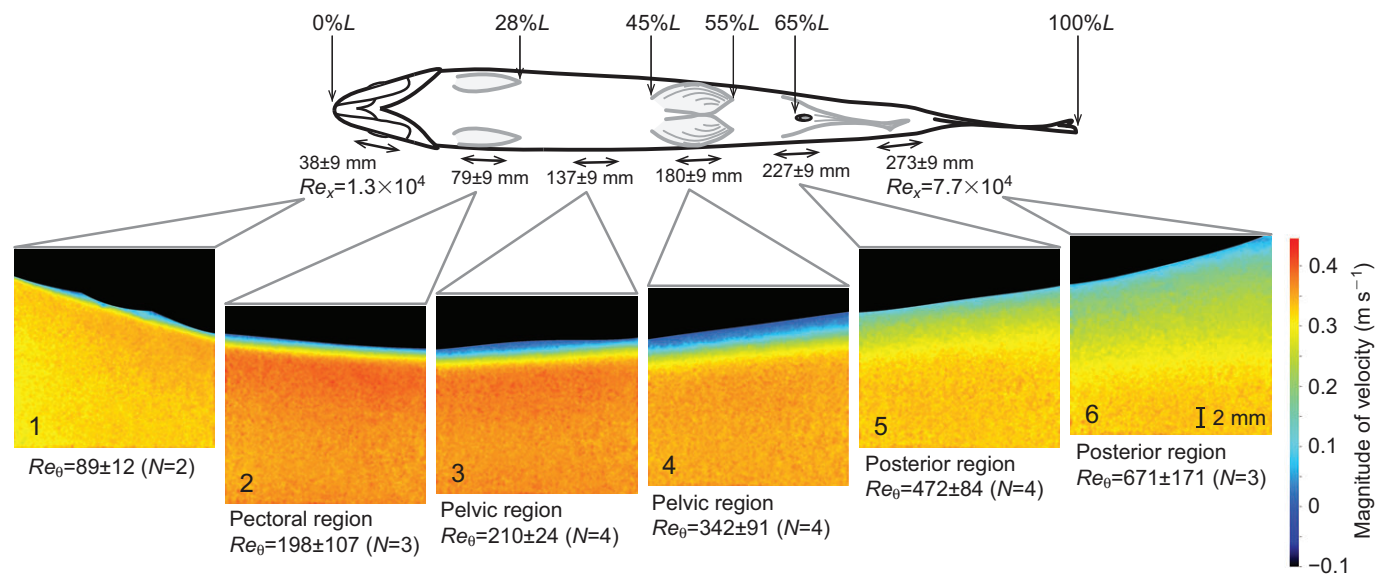
Fig. 2. Velocity fields near the rigid-body surface. Body length (L)=0.305±0.020 m, N=4. The magnitude of the flow velocity in an area of ~18×18 mm² is mapped using colour scales from the head part (image 1; l_x=38±9 mm) to the tail part (image 6; l_x=260±9 mm). Each image of the velocity field is superimposed by a mask image produced by post-particle image velocimetry (PIV) image processing, in which the fish surface was approximated by a fourth-degree polynomial function. Note that there were no PIV data for the anterior body part of the swimming fish corresponding to image 1. The surface region corresponding to each velocity field image is indicated by double-headed arrows with arc-length (±upper or lower bound) of the fish surface measured from the rostrum. The relative position of each reference point (tip of the pectoral fin, base of the pelvic fin, anal and base of the anal fin) to the body length is indicated by %L. Re_x represents a Reynolds number based on the arc-length (l_x) of the fish surface from the rostrum and free-stream velocity. Re_θ represents the Reynolds number based on the momentum thickness and the maximum flow velocity in the exterior flow field near the edge of the boundary layer.

profile (u^+=0.41^{-1}ln y^++5.0+Δu^+, Δu^+=4.0±0.7, n=4). The edge of the boundary layer (δ) corresponds to y^+=82±19 (n=4). In the subsequent concave-motion sequence with five image pairs (100 Hz), the mean u^+ in the inner layer (20<y^+<60 or 24% δ<y<71%δ) revealed an asymptotic profile to the classical logarithmic law-of-the-wall line, u^+=0.41^{-1}ln y^++5.0. However, Spalding's inner law expression (Eqn 2) did not permit mathematical prediction of the mean u^+ in the spectrum (the buffer layer: 5<y^+<20) between the viscous sub-layer and log-law layer. At greater distances from the fish surface, the mean u^+ profile velocity exceeded the classical logarithmic law-of-the-wall line in a wake-like shape (Δu^+=u^+−$u^+_{log-law}$). This wake-like structure is described by the so-called wake function,

$$w\left(\frac{y}{\delta}\right) = \sin^2\left(\frac{\pi}{2}\frac{y}{\delta}\right),\qquad(3)$$

so that the deviation is normalized to zero at the surface and unity at y=δ. Thus, the velocity profile in the log-law region and the outer region is described using a composite formula,

$$u^+ = \frac{1}{\kappa}\ln y^+ + B + \frac{2\Pi}{\kappa}w\left(\frac{y}{\delta}\right),\qquad(4)$$

where Π is called Coles' wake parameter (Coles' log-wake law, 1956). The Δu^+_{max} occurred at 101%δ. This corresponded to y^+=98. Curve fitting [the generalized reduced gradient (GRG) algorithm for a non-linear optimization; Microsoft Excel Solver, Microsoft, Redmond, WA, USA] of the empirical data to the logarithmic overlap (20<y^+<60) and the outer layers (y^+>60) yielded Π=0.21 (R^2=0.99, P<0.01). The quantity Π accounts for the effect of the longitudinal pressure gradient along the fish surface (dp/dx) on the boundary layer profile and is related to the equilibrium pressure gradient parameter: β=($\delta^*\tau_0^{-1}$)(dp/dx) (Clauser, 1954, 1956) by the

approximate correlation given by Das (1987):

$$\beta = -0.4 + 0.76\Pi + 0.42\Pi^2.\qquad(5)$$

Using this equation, β in this concave-motion sequence was calculated to be −0.22.

Following the Newtonian-like, turbulent boundary layer profile (Eqn 4), the mean u^+ profile shifted below the classical log-law line in the remainder of the concave-motion sequence (Fig. 8B). The effect of non-zero normal velocity (v_w) at the surface adds a strong streamwise convective acceleration, $v_w(\partial u/\partial y)$ to the boundary layer flow (White, 1991). Stevenson (1963) modified the classical logarithmic law of the wall and discovered the following relationship, depending on wall suction (v_w<0) or injection (v_w>0):

$$\frac{2}{v_w^+}[(1 + v_w^+u^+)^{1/2} - 1] = \frac{1}{\kappa}\ln y^+ + B,\qquad(6)$$

where v_w^+=$v_wU_\tau^{-1}$. The v_w^+ that was estimated from a series of 14 image pairs (n=14; 100 Hz) during the corresponding concave-motion sequence was −0.09±0.16 (a least squares approximation). The mean u^+ profile oscillated in response to the change in non-zero v_w^+ immediately before the end of this concave-motion sequence. The average τ_0 during this period was 0.448±0.034 Pa (n=14). This significantly exceeded the value determined during the aforementioned periods at a confidence level of 95% (Steel–Dwass test). Depending on the oscillatory cycle and positions, this state continued for several image pairs after the subsequent convex-motion phase began. Hence, the non-Newtonian flow profile (i.e. Virk's asymptote) in the convex-motion phase lasted no longer. The time-average τ_0 during such a convex-motion sequence was somewhat greater. However, the qualitative characteristics of the mean u^+ profile behaviour were generally the same across surface regions unless flow separation occurred.
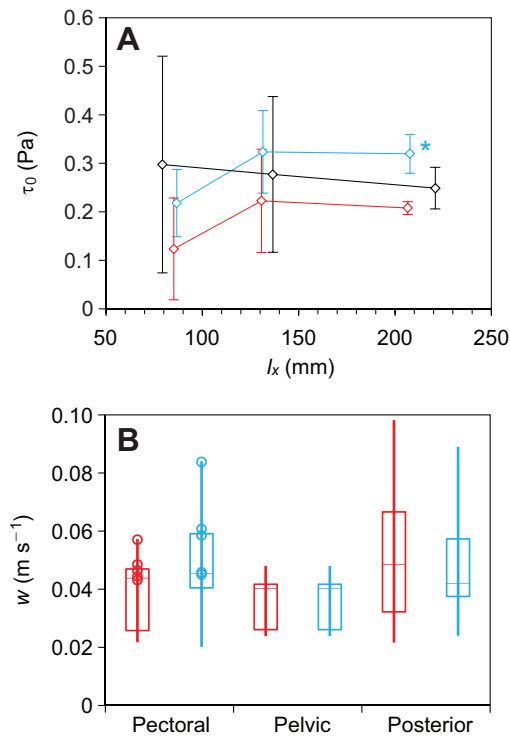
Fig. 3. Wall shear stress (τ_0) and magnitude of the normal component (w) of transverse surface velocity measured at three body regions. Data points from left to right represent pectoral, pelvic and posterior regions. The local Reynolds numbers, Re_x, based on the arc-length (l_x) of the fish surface measured from the rostrum are 2.9×10^4 in the pectoral region, 4.6×10^4 in the pelvic region and 6.7×10^4 in the posterior region. (A) The plot compares the τ_0 of swimming fish in the convex-motion phase (red; pectoral: $N=2$, pelvic: $N=3$, posterior: $N=3$), the concave-motion phase (blue; pectoral: $N=3$, pelvic: $N=4$, posterior: $N=15$) and the rigid-body case (black; pectoral: $N=2$, pelvic: $N=3$, posterior: $N=3$). Convex-motion phase versus concave-motion phase: blue asterisk, significant at $P<0.05$. The error bars represent s.d. from the mean. (B) Distribution of w in each surface region (pectoral, pelvic, posterior) is expressed by the box plots and is compared with the convex-motion phase in red [pectoral: number of observations (n)=8 from two fish, pelvic: $n=5$ from three fish, posterior: $n=15$ from three fish] and the concave-motion phase in blue (pectoral: $n=8$ from two fish, pelvic: $n=4$ from three fish, posterior: $n=15$ from three fish). Boxes are defined by the first and third quartile values. The total range of values appears as vertical bars. The horizontal bar in the box represents the median. The w in the convex-motion sequence where flow separation occurred and in the neighbouring concave-motion sequences is plotted as red and blue circles, respectively.

DISCUSSION

### Interspecies comparison of boundary layer characteristics

Anderson et al. (2001) previously measured the unsteady boundary layer of two species, the scup (*Stenotomus chrysops*) and the dogfish (*Mustelus canis*), with different swimming methods, namely carrangiform and anguilliform modes. The streamwise trends of boundary layer-related variables, such as U_e/U, δ, τ_0 and C_{fx}, and local oscillations with the same variables and the overall profile of these species are comparable to those of rainbow trout. The streamwise trend of the U_e/U ratio reflects the effect of mean streamwise acceleration of the near-field flow, which was superimposed by the local oscillatory acceleration associated with the transverse surface motion, on the behaviour of these variables (Anderson et al., 2001). The U_e/U ratio in the pectoral to pelvic regions of swimming rainbow trout was more pronounced than that of scup at a comparable position ($x=0.5L$). However, the U_e/U ratio of dogfish at $x=0.7L$ was much greater than that of rainbow trout in a comparable position. We attribute these
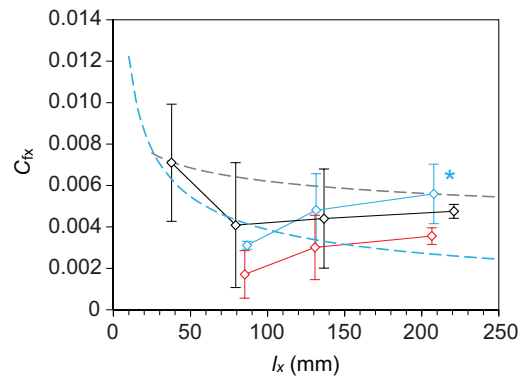
Fig. 4. Local friction coefficient (C_{fx}). The plots compare the C_{fx} of swimming fish in the convex-motion phase (red; pectoral: $N=2$, pelvic: $N=3$, posterior: $N=3$), the concave-motion phase (blue; pectoral: $N=2$, pelvic: $N=3$, posterior: $N=3$) and the rigid body case (black; $l_x=38\pm9$ mm region, $N=2$; pectoral: $N=3$, pelvic: $N=4$, posterior: $N=4$). There were no PIV data for the swimming fish that were comparable with the anterior surface of the rigid body ($l_x=38\pm9$, $N=2$). Convex-motion phase versus concave-motion phase: blue asterisk, significant at $P<0.05$. The blue and grey dashed lines represent C_{fx} of a flat plate estimated theoretically, assuming laminar and turbulent boundary layers, respectively. The local Reynolds numbers, Re_x, based on the arc-length (l_x) of the fish surface measured from the rostrum are 2.9×10^4 in the pectoral region, 4.6×10^4 in the pelvic region and 6.7×10^4 in the posterior region. The error bars represent s.d.

differences to the species-specific difference in swimming methods of rainbow trout and the two species tested by Anderson et al. (2001) as they explain the difference between scup and dogfish. Based on the classification of the body area that is utilized for significant propulsion while swimming, sub-carrangiform swimming for rainbow trout falls into the spectrum of body and caudal fin (BCF) propulsors between carrangiform and anguilliform swimming. Anguilliform swimming is at one extreme where the anterior body area contributes more to providing rearward transfer of momentum to the water (Webb, 1984). Thus, this difference appears to be directly reflected in the difference among the U_e/U ratios of the three species.

Anderson et al. (2001) explained that the skin friction increase in the posterior body part of the dogfish with decreasing δ was a realization of the boundary layer thinning hypothesis (Lighthill, 1971). As shown in Fig. 5, the δ of rainbow trout was instantaneously minimized as would be expected in a boundary layer under an accelerating exterior flow, where the U_e/U ratios tended to be maximized. However, the distribution wave of the C_{fx} in rainbow trout oscillated at roughly π out of phase with that of the dogfish (see fig. 11 in Anderson et al., 2001). This phase discrepancy is attributed partly to the flow separation that did not occur in Anderson et al. (2001), but occurred exclusively in the pectoral region of rainbow trout and the polymeric flow-like profile (Fig. 8A) that was revealed in entire surface regions during the convex-motion sequence. At the mid-point of this time sequence, the wall shear stress (τ_0) approached zero. Hence, the time-averaged C_{fx} became smaller. In contrast to that of the scup and the dogfish, the time-averaged C_{fx} of rainbow trout in the concave-motion phase (the trough-motion phase in Anderson et al., 2001) exceeded that in the convex-motion phase (the crest-motion phase in Anderson et al., 2001). It is interesting to note that this trend agrees qualitatively with time-dependent simulations of skin friction at comparable positions over the surface of a moving flat plate, emulating aquatic animal locomotion, by Ehrenstein and Eloy (2013; see fig. 16 in their paper). The body-motion phase (ϕ) at the maximum peak C_{fx} in rainbow trout was fixed in the third quadrant in Fig. 5 throughout the
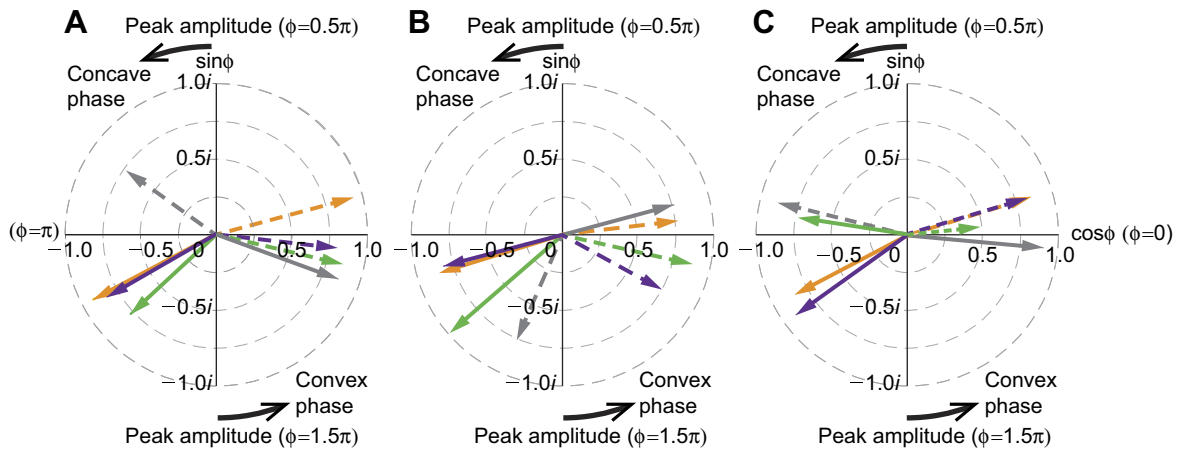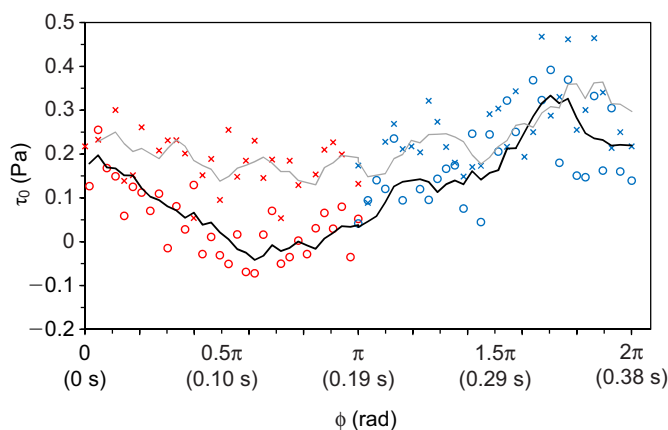
Fig. 5. The relationship between boundary layer-related parameters and phase (φ) of surface movement. The vertical displacement of the oscillatory fish surface is modelled with a sine wave. The peak displacements of the convex and concave surface correspond to $\phi=0.5\pi$ and $\phi=1.5\pi$, respectively. Phase (ϕ) of the surface movement, at which the maximum value (solid arrows) and the minimum value (dashed arrows) were recorded in (A) the pectoral, (B) the pelvic and (C) the posterior surface regions are indicated by the azimuth projected on a complex plane. The phase vectors for the ratio of the maximum flow velocity out of the edge of the boundary layer to the free-stream velocity (U_e/U), wall shear stress (τ_0), local friction coefficient (C_{fx}) and boundary layer thickness (δ) are indicated in grey, violet, orange and green, respectively. Time and phase increase in a counter-clockwise direction. At $\phi=0$ and π, the fish surface passed the mid-point of the time sequence in the convex-motion and concave-motion phases, respectively. The longer the vector length, the more the phase vector is oriented to the direction (one-sidedness).

entire surface regions that were measured. This was immediately after the fish surface passed the mid-point ($\phi=\pi$) of the time sequence in the concave-motion phase, whereas a clockwise phase procession of the maximum C_{fx} was observed in the dogfish. The present study limited the capability to measure the travelling body wave. However, this inter-species difference depends on the relationship between wavelengths of the undulatory body wave

Fig. 6. Comparison of the temporal variation in the wall shear stress (τ_0) at the fish surface in the pectoral region between the fish with and without flow separation. The data plots show temporal variation in the average τ_0 during one complete cycle of transverse surface motion, in which flow separation occurred in the convex-motion phase (red circles) followed by the concave-motion phase (blue circles) and did not occur in the convex-motion phase (red crosses) followed by the concave-motion phase (blue crosses). The number of observations (n) was five for the with- flow separation sequence and three for the without-flow separation sequence. The cycle time was normalized by the average phase duration of 0.381 ± 0.004 s ($N=2$). The average τ_0 for each individual fish (with and without flow separation) was taken at every 0.1 rad phase angle from the beginning of the convex-motion phase ($\phi=0$) to the end of the concave-motion phase ($\phi=2\pi$). Negative τ_0 values are suggestive of flow separation. To smooth the data series, variations in the 5-data moving average are indicated by a black line for the fish with flow separation and a grey line for the fish without flow separation.
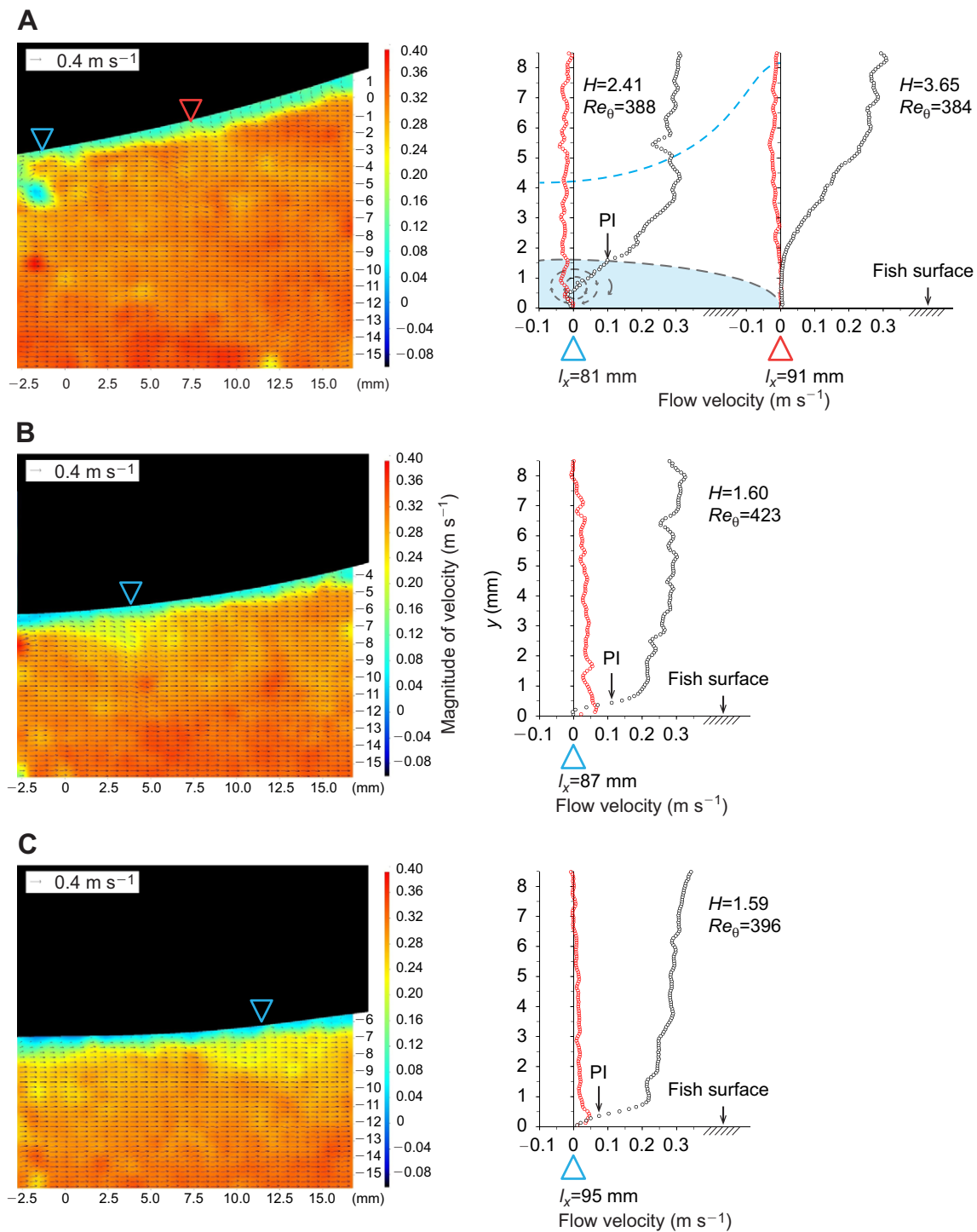
and distribution wave of the C_{fx} that can travel in a single cycle of surface movement. This means that the distribution wave of the C_{fx} in rainbow trout, which can be represented as a travelling wave moving in the same direction as the undulatory body wave, is similar in frequency (f), wave-length (λ) and thus wave velocity (c) to the travelling body wave, as $c=f\lambda$.

The empirical C_{fx} in the pectoral region in both the convex- and concave-motion phases deviates from theoretical estimates for laminar and turbulent boundary layers on a flat plate (Fig. 4). This makes it difficult to predict an unknown C_{fx} on the anterior surface of swimming rainbow trout by extrapolating empirical data in the downstream regions. Indeed, the C_{fx} of swimming rainbow trout in the concave-motion phase significantly exceeded that in the convex-motion phase only in the posterior region. However, as Fig. 4 shows, the difference may be cancelled entirely in one cycle of the surface movements by the skin friction reduction that occurred at the same time on the contralateral side of the fish surface in the convex-motion phase. Therefore, an undulatory surface motion between the pectoral and posterior regions contributed nothing to the total increase in skin friction in these regions relative to the rigid-body case. Even though the unknown C_{fx} upstream of the pectoral region can increase to a theoretical estimate for a stationary flat plate in the case of a turbulent boundary layer, regardless of flow separation, it is possible that the skin friction increase due to undulatory motion will be less than the estimate (20%) based on the time-dependent simulations for a moving flat plate emulating aquatic animal locomotion by Ehrenstein and Eloy (2013). The above findings and the lack of streamwise acceleration in the posterior region, in contrast to the dogfish case, suggest that a 1.9-fold (in the dogfish case) or even 3- to 5-fold skin friction increase (based on the Bone–Lighthill boundary layer thinning hypothesis) relative to the rigid-body case is extremely unlikely under the conditions that are present in this study.

The mean u^+ profile during the intermediate to later phase in the convex-motion sequence (black crosses in Fig. 8A) showed a structure similar to that achieved in experimental demonstrations and computer-based simulations for drag reduction by adding high molecular weight polymers to wall-bounded turbulent flows in

Fig. 7. Velocity vector field and boundary layer profiles at different time points. (A) When flow separation was first identified, and (B) nine frames (0.045 s) and (C) 15 frames (0.075 s) after the flow separation was first identified. A mask image was overlaid on the velocity vector field image in order to disable any data in the region corresponding to the fish body (black region). Note that the colour scales represent the magnitude of the flow velocities in the reference frame of the flow channel. The boundary layer profile plots the vertical gradient of tangential (u, black circles) and normal velocities (v, red circles) at a given position over the fish surface. y, surface-normal distance. (A) The u and v profiles were measured over the fish surface at an arc-length (l_x) of 81 mm and at l_x=91 mm from the rostrum. The former is directly below the centre of the vortex core and the latter is the position of zero shear stress. The rough positions at l_x=81 and l_x=91 mm are indicated in the velocity vector field image. The recirculation region that is suggestive of a laminar separation bubble is shaded blue. Grey arrows represent the direction of the flow. The dashed blue line represents the edge of the detached shear layer. PI represents a point of inflection. (B) The u and v profiles were measured at l_x=87 mm, which is directly below the centre of the vortex core. The rough position at l_x=87 mm on the fish surface is indicated in the velocity vector field image. (C) The u and v profiles were measured at l_x=95 mm, which is directly below the centre of the vortex core. The rough position at l_x=95 mm on the fish surface is indicated in the velocity-vector-field image. H represents the shape factor. Re_θ represents the Reynolds number based on the momentum thickness and the maximum flow velocity in the exterior flow field out of the edge of the boundary layer.
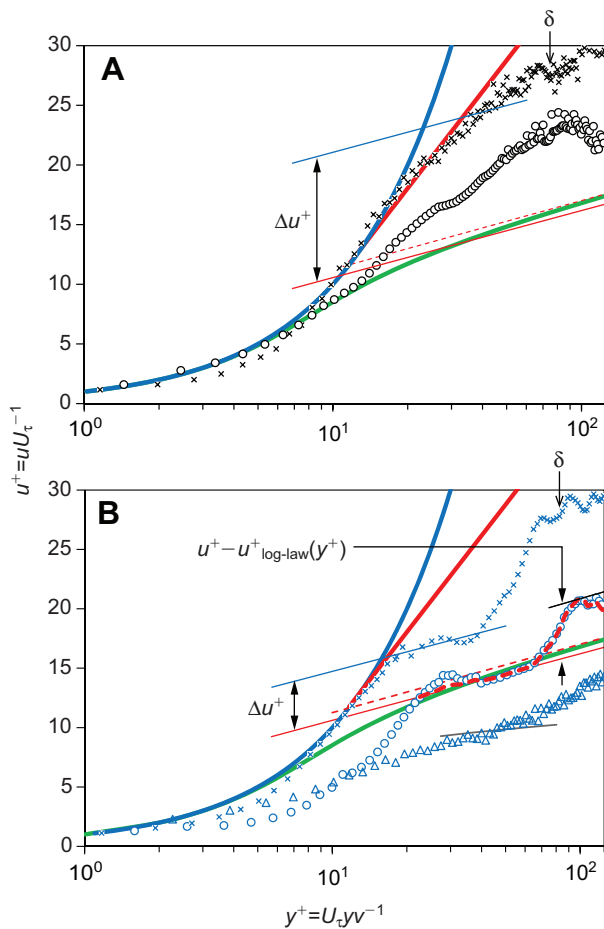
Fig. 8. Unsteady boundary layer profile envelope in the posterior surface region during one complete oscillatory cycle of surface movement. Here, l_x=240±4 mm, n=46 image pairs. The solid blue curve represents the linear law ($y^+=u^+$). The thin solid and dashed red lines represent the classical logarithmic law of the wall (log-law) line: $u^+=\kappa^{-1}\ln y^++B$ in the case of κ=0.41 and B=5.0 (Schlichting, 1979), and κ=0.40 and B=5.5 (Coles and Hirst, 1968), respectively. The green curve represents Spalding's law of the wall (1961). The Virk's asymptote (Virk, 1975): u^+=11.7 ln y^+−17 is indicated by a bold red line for reference. The log-law line that is pushed by Δu^+ away from the fish surface is indicated by a thin blue line. (A) Black circles and black crosses represent the mean u^+ profiles resolved from a series of five image pairs (n=5) in the beginning phase of the convex-motion sequence (100 Hz) and a series of 18 image pairs (n=18) in the remainder of the convex-motion sequence (100 Hz), respectively. (B) Blue crosses, blue circles and blue triangles represent the mean u^+ profiles resolved from a series of four image pairs (n=4) in the early phase of the concave-motion sequence (100 Hz), a series of the subsequent five image pairs (n=5) during the concave-motion phase (100 Hz) and a series of 14 image pairs (n=14) in the remainder of the concave-motion sequence (100 Hz), respectively. The bold dashed red line represents the law of the wall, in which Coles' law of the wake (1956) is embedded in order to describe an S-shaped wake ($u^+-u_{\log-law}^+$). The grey line represents the new law with a mean v_w^+ of −0.09±0.16 (n=14). l_x is the arc-length of the fish surface from the rostrum and U_τ is the friction velocity. v_w^+ is the non-zero normal velocity at the surface, δ is the boundary layer thickness and ν is the kinematic viscosity of water.

engineering research (Virk, 1975; L'vov et al., 2004; Benzi et al., 2006). It is believed that the mean u^+ profile in the early phase of the concave-motion sequence (blue crosses in Fig. 8B) retained some memory of the previous history of the lower mean flow velocity in the later phase of the convex-motion sequence. During these periods, the boundary layer profile realized a particularly small degree of wall shear stress (τ_0), which represents a state of near

separation (i.e. incipient separation). As Anderson et al. (2001) suggested, how rainbow trout can capitalize on this benefit, but with less pressure drag than if the flow separated from the surface, is considered to be a key strategy for drag reduction.

As illustrated in Fig. 8, the wake-shape velocity fluctuation extending in the internal turbulent boundary layer represents a strong interaction between the free-stream turbulence and boundary layers. Furthermore, it is possible that turbulence transition would occur at a lower Re_x than the critical range [Re_x=3.5–5.0(×10^5)] in a flow environment that has a turbulence intensity greater than 0.001 (Schlichting, 1979). Preston (1958) proposed a momentum thickness Reynolds number (Re_θ) of 320, above which the flow is likely to be fully turbulent. The Re_θ in swimming rainbow trout exceeded this critical value across the entire surface regions that were measured. Regardless of the position and direction of the surface movement, the shape factor (H) of the boundary layer profiles showed convergence around 1.62±0.07 (N=8) and 1.56±0.09 (N=8) in the convex-motion and concave-motion sequences, respectively. These H values are closer to the value of 1.3 based on the 1/7th power law turbulent velocity distribution than to the value of 2.59 based on the so-called Blasius profile for a laminar boundary layer (Schlichting, 1979). If taken together, these observations explain why, unlike what was observed in Anderson et al. (2001), the boundary layer profile of rainbow trout did not permit good approximation by the known laminar boundary layer profile.

In summary, we characterized the boundary layer over the surface of swimming rainbow trout as streamwise trends and local oscillations in the boundary layer-related parameters that behaved like an out-of-phase wave with transverse surface movement. The boundary layer profile showed unsteadiness, oscillating above and beneath the log-law: u^+=0.41^{-1}ln y^++5.0 in the classical law of the wall for a turbulent boundary layer. There was no definitive evidence to support the Bone–Lighthill boundary layer thinning hypothesis (Lighthill, 1971) that attributes high power requirements of undulatory swimming to drag enhancement. The wall shear stress tended to approach zero on the convex surface around the mid-point of the time sequence, while the fish surface was moving towards the free-stream flow. Thus, the time-averaged skin friction was locally dampened on the convex surface. However, the skin friction was amplified on the concave surface during the retreat of the fish surface. These findings contradicted previous findings in different species measured by Anderson et al. (2001), but offer insight into drag reduction strategies employed by rainbow trout in a turbulent flow environment. Demonstrating the effect of mucus on the skin friction reduction has proved elusive in the present study. The reason for this is that the physical properties of the mucus concentration in the viscous sublayer, which consists partly of high molecular weight polymers that are soluble in water (Daniel, 1981), are uncertain. Therefore, further work is necessary to clarify the speculation about the effect of fish skin mucus on drag reduction. This approach definitely should be explored in the future.

Flow separation and implications for lateral-line flow sensing
Flow separation was the most notable event that differentiated swimming rainbow trout from the two species tested by Anderson et al. (2001). A small recirculation region near the fish surface (Fig. 7A) that was created by flow separation resembles a laminar separation bubble (Gaster, 1967). Laminar separation bubbles occur when the previously attached laminar boundary layer encounters an adverse pressure gradient of sufficient magnitude to cause the flow to separate (O'Meara and Mueller, 1987). The disturbance level of the near-field flow upstream of the pectoral

region would not have been high without local oscillatory acceleration associated with the transverse surface motion because the momentum thickness Reynolds numbers (Re_θ) upstream of the pectoral region of the rigid body surface were far smaller than the value for the onset of the laminar-to-turbulent transition (Re_θ=320). Not surprisingly, the transverse surface velocity became greater with increasing arc-length (l_x) from the rostrum because the propulsive surface near the tail travels a greater distance in the same period of oscillatory motion than does the anterior body surface (Triantafyllou et al., 2002). However, the significantly increased magnitude of the normal component (w) of surface velocity during both the convex-motion sequence with flow separation and the neighbouring concave-motion sequences (Fig. 3B) suggests that self-generated hydrodynamic perturbation caused the flow separation. Hydrodynamic perturbations from flow over the fish body in a horizontal plane can cause translational disturbance, side slip for lateral displacement or rotational disturbance, and yaw for rotation to the left/right about a vertical axis (Webb, 2004b). Because the entire cycle of the surface movement occurred within a fixed view field as small as 20×20 mm², one cannot reasonably assume that the fish experienced a side-slip disturbance. Therefore, one can interpret the incidence that occurred in our rainbow trout as follows. As a result of the self-generated rotational disturbance (yaw), incident vortices of sufficient magnitude that had been shed backwards from the leading edge would interact with the boundary layer flow or fish surface that was moving towards the free-stream flow at a faster w when they were encountered. This interaction should cause considerable unsteadiness of the structure of the boundary layer that previously attached to the fish surface, thereby leading to flow separation. Normal mass flux from free-streaming into the detached shear layer (i.e. negative velocity v at the outer edge, Fig. 7A) could enhance the momentum transfer in the detached shear layer and, consequently, increase the thickness of the detached turbulent shear layer. Shortly thereafter, with phase transition of transverse surface movement from a convex- to concave-sequence posteriorly, the pressure downstream of the separation point was progressively directed downstream (favourable pressure gradient). This is supported by a negative value of the equilibrium pressure gradient parameter $\beta = (\delta^* \tau_0^{-1})(\mathrm{d}p/\mathrm{d}x)$ in the early phase of concave-motion sequence. One can assume that, along with increased thickness of the detached shear layer, a progressive change in the pressure gradient near the fish surface from adverse to favourable would facilitate reattachment of the detached shear layer to the fish surface immediately downstream from the separation point by eliminating the reversed flow direction in the separation bubble (O'Meara and Mueller, 1987).

Provided that lateral-line afferents that innervate the hair cells in a single superficial neuromast are flow sensitive, the reversed flow that was observed immediately upstream of the reattachment point (Fig. 7A) could cause a time-shifted irregular pattern of neuronal signals from a superficial neuromast in the reverse-flow region unlike those in upstream and downstream regions. Of course, there is the possibility that the observed recovery from flow separation was due to self-correction without sensory input. Whatever the reason, the immediate recovery must have influenced swimming performance more favourably than if the reattachment was delayed until further downstream to the trailing edge. In the latter case, the wake-induced unsteadiness, pressure fluctuations, structure vibrations and noise would have been further increased within the separated shear layer and the reattachment region (Troutt et al., 1984). It is uncertain how the temporal patterns of lateral-line afferent discharge respond to the physical act of shear flow that behaves in an out-of-phase
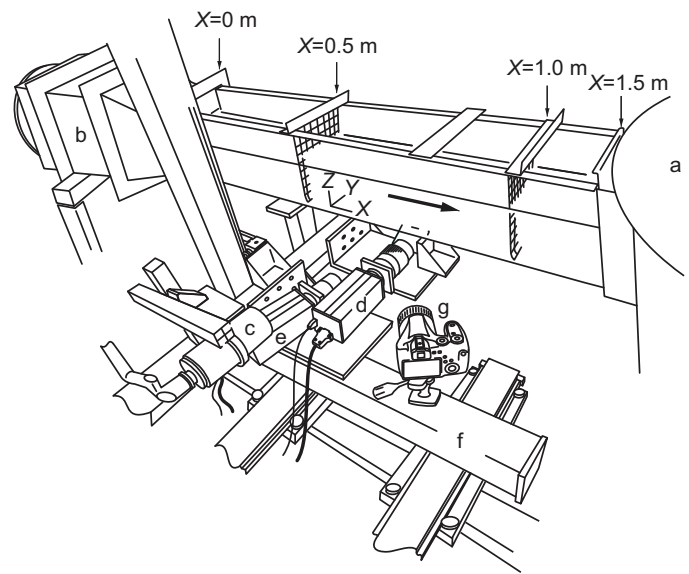
Fig. 9. An overview of the experimental setup. The boundary layer of rainbow trout swimming in a working section (X=0.5–1.0 m) was measured using the PIV technique. The flow drawn from a settling tank (a) was delivered to the open channel after the flow area was reduced at a contraction (b) directly upstream of the open channel. The arrow represents the direction of a seeded flow. PIV images were acquired in a horizontal mid-plane of the fish illuminated from the side using a Nd:YLF pulsed laser through light sheet optics (c) and imaged from the bottom by a mirror using two high-speed cameras, which are described as a boundary layer camera (d) and a near-field camera (e). These cameras were mounted on a motor-driven slider (f). A lateral view of the swimming behaviour of the fish was recorded simultaneously using a high-speed camera (g). The X-axis, which is oriented in the stream-related direction, represents distance from the inlet of the flow channel (X=0); the Y-axis, which is oriented in the span-related direction, represents distance from the right wall of the test section determined by facing downstream; and the Z-axis, which is oriented in the floor-normal direction, represents the height from the floor of the test section.

waveform with surface movement and how they are perturbed by flow separation. To answer these questions, we require an inter-disciplinary approach that incorporates a neurophysiological technique into the present capabilities of hydrodynamic studies. This is a key objective of future studies.

MATERIALS AND METHODS
Fish
Rainbow trout were obtained from a fish farm (Pohtiolampi Osprey Centre, Kangasala, Finland). The fish were held indoors in a 300 l aquarium at the Flow Research Laboratory of Tampere University of Technology, Finland. The water in the holding tank was sufficiently oxygenized and maintained in an appropriate condition while being recirculated through a filtration system.

Experimental flow system
Unidirectional flow was induced in a 1.5 m open channel of the recirculating flow system (Fig. 9) by drawing the water from a settling tank (2 m²) that was located downstream of the open channel using a centrifugal pump (AHLSTAR, Sulzer, Kotka, Finland). Fine mesh screens and a stainless steel honeycomb that were located in a contraction directly upstream of the open channel provided strong damping of the flow disturbance over the cross-sectional area of the test section. Assuming that the turbulence in the free-stream flow was isotropic, the turbulence intensity (T) is defined as $T = u_{rms}/U$, where u_{rms} is the root mean square of the fluctuating velocity component in the free-stream direction (Schlichting, 1979). T in the free-stream flow (U=0.311 ±0.027 m s⁻¹) that was measured using the PIV technique at 16 positions of different depths (0.04−0.08 m from the bottom) in a 0.21×0.24×0.50 m
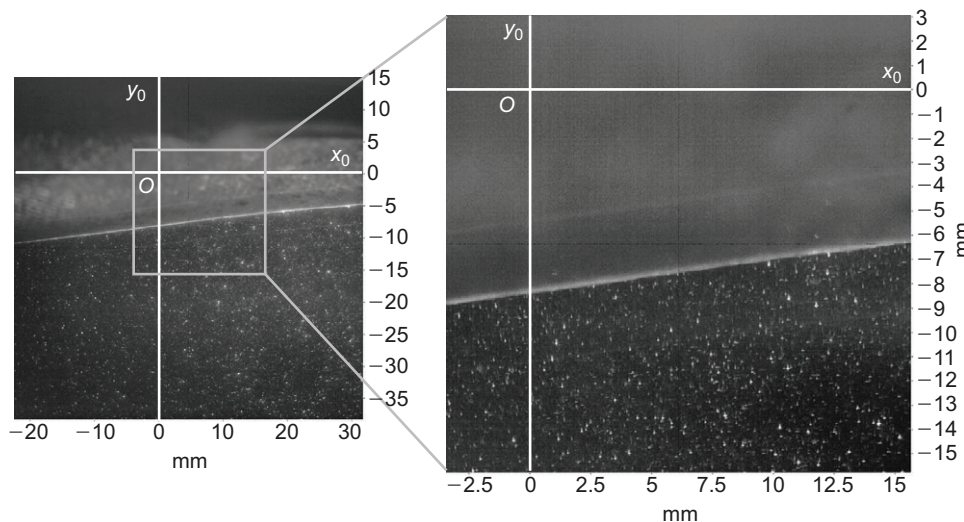
Fig. 10. PIV images acquired from two cameras for imaging the boundary layer and the near field affected by the presence of the boundary layer, and definition of the 2D-coordinate system shared by the two cameras. Left image, near-field camera; right image, boundary-layer camera. The area in the white square in the left image is enlarged in the right image. The positive x_0 direction represents the free-flow direction associated with tangential velocity (u) relative to the fish surface. The transverse surface movements in the positive y_0 direction and negative y_0 direction are described as concave motion and convex motion, respectively, in the text.

(width×height×length) test section (without fish) was 4.7±0.7%. The volumetric flow rate did not change during the experimental trials. Consequently, the depth of water in the test section was maintained at 0.12 m. The water temperature was maintained at 20°C.

To facilitate the station-holding behaviour of the swimming fish (1.02± 0.09 $L\,s^{-1}$, N=4), a transparent Plexiglas wall of the test section was marked with black stripes that were spaced at 5.0 cm intervals as a visual reference. The solid blocking effect is known as a phenomenon in which the presence of the fish in an enclosed flow channel increases the flow velocity around the fish (Bell and Terhune, 1970). However, the cross-sectional area of the fish was less than 10% of the cross-sectional flow area of the open channel. Therefore, no correction of the flow velocity was necessary (Brett, 1964).

PIV image acquisition condition

A rainbow trout was constrained to swim in the test section. After an hour of acclimation of the fish to the experimental environment, PIV images were acquired from the bottom of the test section by use of a mirror that was angled at 45 deg and two high-speed cameras (ImagerProHS, LaVision, Göttingen, Germany). A number of singly exposed particle image pairs with a resolution of 1040×1024 pixels were recorded simultaneously by the cameras at 200 frames s^{-1}. The flow field that was seeded with neutrally buoyant tracer particles was illuminated by a horizontal laser sheet with a pulse delay of 300 µs (Nd:YLF pulsed laser, ESI New Wave Division, Cambridge, UK). We chose seeding particles with diameters as small as 10 and 20 µm (glass spheres, LaVision) to ensure an adequate tracer response of the particles in turbulent flow (Hadad and Gurka, 2013). The laser and the camera with a 20×20 mm^2 view field (approximately) that was used to image the boundary layer, which is described as the boundary layer camera, and the other camera, which has a 50×50 mm^2 view field (approximately) and is described as the near-field camera, were synchronized according to the pulse generated by a software-programmable timing unit (PTU-9, LaVision) under the control of DaVis software (v. 7.2, LaVision). The boundary layer camera completed PIV flow imaging with the use of a 105 mm macro lens (Sigma 105mm f2.8D EX DG, Sigma, Tokyo, Japan) without image distortion. To acquire particle image pairs of a wider flow field from the near-field camera, a 50 mm macro lens (MicroNikkor 50mm f1.2D, Nikon, Tokyo, Japan) was used in combination with a tilt/shift lens adaptor and a teleconverter extension ring (N-AFD 1.5× TLLEPLUS SHQ, Kenko, Tokyo, Japan). The positions of the boundary layer camera and the near-field camera that were mounted on a custom-built motor-driven slider were finely adjustable using the joysticks of a controller (Motionline, Lenord, Bauer & Co., Oberhausen, Germany). To describe the oscillatory motion of the fish surface, we use the term 'convex' and 'concave', depending on the direction of transverse surface movement in an approximately 20×20 mm^2 field of view of the boundary layer camera.

Convex motion describes the situation when the section of the fish surface in the view field of the boundary layer camera was directed in the negative y_0 direction in Fig. 10, while the fish surface was moving towards the free-stream flow. Concave motion describes the situation when the section of the fish surface was directed in the positive y_0 direction in Fig. 10, while the fish surface was retreating from its extreme position after the convex-motion sequence was completed. To locate the position of the laser sheet on the fish, the lateral view of the test section was recorded using a high-speed camera (EX-F1, Casio, Tokyo, Japan). Immediately after PIV flow imaging of the swimming fish, the fish was killed by administration of anaesthetic (emulsified solution of oil of cloves, 5 drops of 100% pure oil of cloves per 4 l of water). PIV measurement was also conducted for the rigid body set in the flow from head to tail at each 0.05 m downstream position.

Post-PIV analysis of boundary layer-related parameters

Post-PIV analysis of boundary layer-related parameters over the fish surface during 1−3 cycles of tail oscillation and the rigid body was conducted on 200−500 quality sequential image pairs that were acquired from each camera per single PIV image-acquisition trial using software custom-written in Matlab (R2012b v.8.0.0.783, MathWorks, Natick, MA, USA). After the targeted PIV image was optimized using the Gaussian filter or average filter to eliminate the noise of the image, the fish surface was separated from the background by the Sobel edge-detection operator in Matlab and approximated by a fourth-degree polynomial function. Every pair of PIV images was analysed using the PIV flow imaging software DaVis (v. 7.2, LaVision), based on a multi-pass interrogation algorithm, where the search window for peak correlation was reduced by three steps from an initial interrogation window size of 32×32 pixels to a final window size of 8×8 pixels, while keeping a 50% overlap. The magnification factors were 18−20 pixels mm^{-1} for the near-field camera and 55−60 pixels mm^{-1} for the boundary layer camera. Therefore, velocity vectors were analysed at 260×256 node points (66,560 vectors) with an equal space of approximately 0.07 mm (4 pixels) in the particle images from the boundary layer camera.

The wall shear stress (τ_0) was estimated from the linear slope of the velocity profiles in the immediate neighbourhood of the surface (Eqn 1 at y=0; Kähler et al., 2006). It was considered to be statistically reliable if this analysis was performed at 100 Hz. However, to identify the temporal position of the flow separation as precisely as possible, where τ_0 passed from positive to negative, further analysis was undertaken at 200 Hz. To eliminate the influence of boundary layers that developed in proximity to the side walls and floor of the flow channel on the accuracy of the estimates for boundary layer-related parameters, sequential image pairs that were acquired between 0.04 and 0.08 m above the bottom of the test section and more than 0.04 m from the side walls of the test section were used for analysis. Computation of the normal distance (d) from a

particular data sampling point to the fish surface was handled as a problem of finding the shortest path between the point and curve. Tangential flow velocity (u) was defined as a velocity component that was parallel to the tangent line at the point on the fish surface where d was determined. Normal velocity (v) was defined as a component of the velocity normal to the tangent line.

The closest approximation of the laminar boundary layer profile is provided by solving the so-called Blasius equation: $f(\eta)f''(\eta)+2f'''(\eta)=0$ (Schlichting, 1979), where the dimensionless coordinate of $\eta=y\delta^{-1}$ is introduced. Assuming that $u/U=f'$, the boundary conditions are determined to be $f'=0$ ($u=0$), $f=0$ ($v=0$) at $\eta=0$ and $f=0$ ($u=U$: free-stream velocity) at $\eta=\infty$. Using the numerical solution (e.g. Howarth, 1938) for $f'(\eta)=0.99$ and the original definition of the local friction coefficient, $C_{fx}=\tau_0/(0.5\rho U^2)$, the C_{fx} and δ for the laminar boundary layer are described as:

$$C_{fx} = 0.664Re_x^{-1/2} \tag{7}$$

and

$$\delta = 5.0l_xRe_x^{-1/2}, \tag{8}$$

where Re_x is the Reynolds number based on the arc-length of the fish surface from the rostrum.

The definition of the boundary layer thickness as $\delta=y(99\%U)$ was arbitrary because it was highly susceptible to the form of the wake section at the edge of boundary layer. Therefore, we also used more meaningful measures physically to describe the boundary layer shape: the displacement thickness, δ^*, and the momentum thickness, θ. They are defined as:

$$\delta^* = \int_0^\infty (1 - uU_e^{-1})dy \tag{9}$$

and

$$\theta = \int_0^\infty uU_e^{-1}(1 - uU_e^{-1})dy. \tag{10}$$

The definite integrals for Eqns 9 and 10 were approximated by adding the areas of rectangles that have a height of approximately 0.07 mm (4 pixels) from the surface to the point where the tangential velocity (u) became the maximum (U_e). The ratio of δ^* to θ is thus:

$$H = \frac{\delta^*}{\theta}. \tag{11}$$

This is called the shape factor, an indicator of a pressure gradient, and hence of a separation tendency. Flow separation is likely to occur at $H\approx3.5$ for a laminar boundary layer and at $H\approx1.8$ to 2.4 for a turbulent boundary layer (Schlichting, 1979).

Using the $\theta\delta^{-1}=7/72$ relationship that was derived from the 1/7th power law turbulent velocity distribution $uU^{-1}=(y\delta^{-1})^{1/7}$ (Schlichting, 1979), the C_{fx} and δ for the turbulent boundary layer are described as:

$$C_{fx} = 0.027Re_x^{-1/7} \tag{12}$$

and

$$\delta = 0.16l_xRe_x^{-1/7}. \tag{13}$$

The results presented in this paper were derived from post-PIV image analyses applied to the measurements over the surface of the swimming fish. They consisted of 28 convex-motion sequences and 27 concave-motion sequences, and the rigid-body surface measurements that comprised 19 PIV trials (Table 1). If not stated otherwise, the boundary layer-related parameters, such as U_e/U, δ, τ_0 and C_{fx}, are presented as a mean±s.d. of all means determined for from different sub-samples within each fish for each of the three surface regions, depending on whether the fish surface was stationary (i.e. rigid-body case) or moving. The measurements collected while the fish was swimming were separated into two groups that reflected the direction of the transverse surface movements (i.e. convex-motion phase or concave-motion phase).

References
Anderson, J. E., McGillis, W. R. and Grosenbaugh, M. A. (2001). The boundary layer of swimming fish. *J. Exp. Biol.* **204**, 81-102.

Batschelet, E. (1981). *Circular Statistics in Biology*. London: Academic Press.

Bell, W. H. and Terhune, L. D. B. (1970). Water tunnel design for fisheries research. *J. Fish. Res. Bd. Can. Tech. Rep.* **195**, 1-69.

Benzi, R., De Angelis, E., L'vov, V. S., Procaccia, I. and Tiberkevich, V. (2006). Maximum drag reduction asymptotes and the cross-over to the Newtonian plug. *J. Fluid Mech.* **551**, 185-195.

Brett, J. R. (1964). The respiratory metabolism and swimming performance of young sockeye salmon. *J. Fish. Res. Board Can.* **21**, 1183-1226.

Clauser, F. H. (1954). Turbulent boundary layers in adverse pressure gradients. *J. Aeronaut. Sci.* **21**, 91-108.

Clauser, F. H. (1956). The turbulent boundary layer. *Adv. Appl. Mech.* **4**, 1-51.

Coles, D. E. (1956). The law of the wake in the turbulent boundary layer. *J. Fluid Mech.* **1**, 191-226.

Coles, D. E. and Hirst, E. A. (1968). Computation of turbulent boundary layers. AFOSR-IFP-Stanford Conference: Compiled data, Vol. II. CA, USA: Stanford University.

Daniel, T. L. (1981). Fish mucus: *in situ* measurements of polymer drag reduction. *Biol. Bull.* **160**, 376-382.

Das, D. K. (1987). A numerical study of turbulent separated flows. In *Forum on Turbulent Flows*, pp. 85-90. Cincinnati, OH: American Society of Mechanical Engineers.

Ehrenstein, U. and Eloy, C. (2013). Skin friction on a moving wall and its implications for swimming animals. *J. Fluid Mech.* **718**, 321-346.

Gaster, M. (1967). The structure and behaviour of separation bubbles. *ARC R. & M.* **3595**, 1-31.

Hadad, T. and Gurka, R. (2013). Effects of particle size, concentration and surface coating on turbulent flow properties obtained using PIV/PTV. *Exp. Therm. Fluid Sci.* **45**, 203-212.

Howarth, L. (1938). On the solution of the laminar boundary layer equations. *Proc. R. Soc. Lond. A* **164**, 547-579.

Kähler, C. J., Scholz, U. and Ortmanns, J. (2006). Wall-shear-stress and near-wall turbulence measurements up to single pixel resolution by means of long-distance micro-PIV. *Exp. Fluids* **41**, 327-341.

Liao, J. C., Beal, D. N., Lauder, G. V. and Triantafyllou, M. S. (2003a). The Kármán gait: novel body kinematics of rainbow trout swimming in a vortex street. *J. Exp. Biol.* **206**, 1059-1073.

Liao, J. C., Beal, D. N., Lauder, G. V. and Triantafyllou, M. S. (2003b). Fish exploiting vortices decrease muscle activity. *Science* **302**, 1566-1569.

Lighthill, M. J. (1971). Large-amplitude elongated-body theory of fish locomotion. *Proc. R. Soc. Lond. B Biol. Sci.* **179**, 125-138.

L'vov, V. S., Pomyalov, A., Procaccia, I. and Tiberkevich, V. (2004). Drag reduction by polymers in wall bounded turbulence. *Phys. Rev. Lett.* **92**, 244503.

McHenry, M. J., Strother, J. A. and van Netten, S. M. (2008). Mechanical filtering by the boundary layer and fluid–structure interaction in the superficial neuromast of the fish lateral line system. *J. Comp. Physiol. A* **194**, 795-810.

O'Meara, M. and Mueller, T. J. (1987). Laminar separation bubble characteristics on an airfoil at low Reynolds numbers. *AIAA J.* **25**, 1033-1041.

Pavlov, D. S., Lupandin, A. I. and Skorobogatov, M. A. (2000). The effects of flow turbulence on the behavior and distribution of fish. *J. Ichthyol.* **40** Suppl. 2, S232-S261.

Preston, J. H. (1958). The minimum Reynolds number for a turbulent boundary layer and the selection of a transition device. *J. Fluid Mech.* **3**, 373-384.

Raffel, M., Willert, C. E., Wereley, S. T. and Kompenhans, J. (1998). *Particle Image Velocimetry: A Practical Guide*, 2nd edn, pp. 1-448. Berlin, Germany: Springer-Verlag.

Schlichting, H. (1979). *Boundary-Layer Theory*, 7th edn, pp. 1-817. New York: McGraw-Hill Book Co.

Spalding, D. B. (1961). A single formula for the "law of the wall". *J. Appl. Mech.* **28**, 455-457.

Stevenson, T. N. (1963). A law of the wall for turbulent boundary layers with suction or injection. The College of Aeronautics, Cranfield, Aero Report 166.1–14.

Triantafyllou, M. S., Techet, A. H., Zhu, Q., Beal, D. N., Hover, F. S. and Yue, D. K. P. (2002). Vorticity control in fish-like propulsion and maneuvering. *Integr. Comp. Biol.* **42**, 1026-1031.

Troutt, T. R., Scheelke, B. and Norman, T. R. (1984). Organized structures in a reattaching separated flow field. *J. Fluid Mech.* **143**, 413-427.

Virk, P. S. (1975). Drag reduction fundamentals. *AIChE. J.* **21**, 625-656.

von Kármán, T. (1930). Mechanische Ähnlichkeit und Turbulenz, Nachrichten von der Gesellschaft der Wissenschaften zu Göttingen. *Fachgruppe 1 (Mathematik)* **5**, 58-76.

Webb, P. W. (1975). Hydrodynamics and energetics of fish propulsion. *Bull. Fish. Res. Board Can.* **190**, 1-159.

Webb, P. W. (1984). Form and function in fish swimming. *Sci. Am.* **251**, 72-82.

Webb, P. W. (2004a). Response latencies to postural disturbances in three species of teleostean fishes. *J. Exp. Biol.* **207**, 955-961.

Webb, P. W. (2004b). Manoeuvrability – general issues. *IEEE J. Ocean. Engin.* **29**, 547-555.

White, F. M. (1991). *Viscous Fluid Flow*, pp. 1-614. New York: McGraw-Hill.